H2020 FET-Open Research and Innovation Actions Project Number 766566
Antiferromagnetic spintronics (ASPIN)

Work package 3, Deliverable D3.2: Report on topological Dirac/Weyl band crossings in antiferromagnets

This report summarizes the work of the ASPIN project consortium exploring the topological features in the electronic structure of antiferromagnets. We also give references to our corresponding publications containing additional information. The teams' contributions to this work were as follows:

- Institute of Physics in Prague (IOP): Materials growth and characterization
- University of Nottingham (NOT): Materials growth and characterization
- Max-Planck Institutes (MPG): Theory
- Johannes Gutenberg University in Mainz (JGU): Materials growth and characterization, theory

Contents

1 Antiferromagnetic Dirac band crossings

Spin-orbitronics and Dirac quasiparticles are two fields of condensed matter physics initiated independently about a decade ago. Here we demonstrate that Dirac quasiparticles can be controlled by the spin-orbit torque reorientation of the Néel vector in an antiferromagnet, using CuMnAs and Mn_2Au as examples [1, 2]. We identify the non-symmorphic crystal symmetry protection of Dirac band crossings whose on and off switching is mediated by the Néel vector reorientation. We predict that this concept, verified by density functional calculations in the CuMnAs and Mn_2Au, can lead to a topological metal-insulator transition driven by the Néel vector and to the topological anisotropic magnetoresistance.

1.1 Topological metal-insulator transition and anisotropic magnetoresistance in CuMnAs

We performed full-potential relativistic *ab initio* calculations of the electronic structure of CuMnAs, as implemented in FLEUR and ELK packages. The exchange correlation potential is parametrized

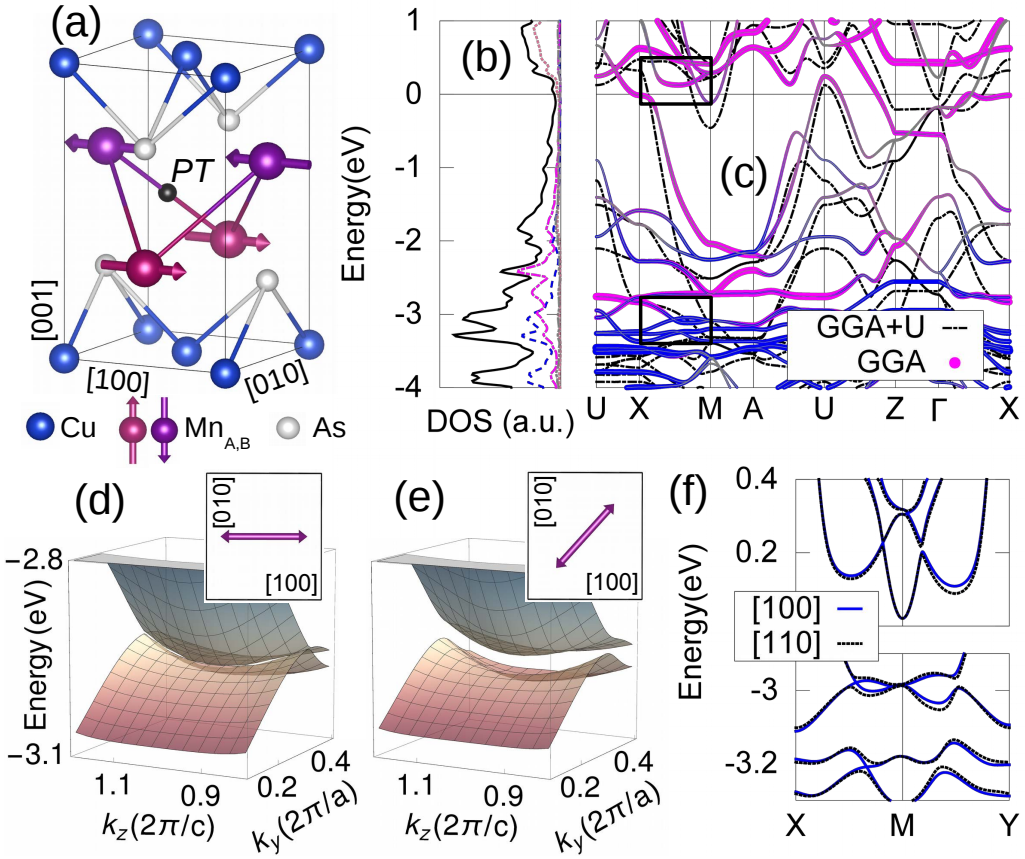

Figure 1: (a) Crystallographic and magnetic structure of the tetragonal CuMnAs. Atom-resolved (b) density of states with semi-metallic pseudogap, and (c) band structure without SOC within GGA. GGA+U shows DPs position shifts. Colors correspond to the atomic colors in (a). Electric control by the Néel SOT of the 3D band dispersion around nodal line along the $k_x = \pi$ BZ sub-manifold calculated by GGA+SOC, which is (d) protected for $\mathbf{n}|[100]$ by glide mirror plane, (e) gapped for $\mathbf{n}|[110]$. $a = b \neq c$ are the lattice constants. (f) Cut along the XMY line through the nodal lines at different energies.

by the Perdew-Burke-Ernzerhof generalized gradient approximation (GGA) [3]. The full crystal of tetragonal CuMnAs, including also the Cu and As atoms, is shown in Fig. 1(a) [4, 5]. Results without spin-orbit coupliong (SOC) are summarized in Figs. 1(b),(c). They show the semimetallic character with the dip in the density of states near the Fermi level and numerous band crossings. Note that their position is sensitive to the computational details; as an illustration we plot in Fig. 1(c) shifted bands obtained in the GGA+U approximation with the correlation potential $U = 3$ eV. When SOC is included in the *ab initio* calculations and the Néel vector $\mathbf{n}\|[100]$, protected nodal lines are obtained in the $k_x = \pm\pi$ planes, as illustrated in Figs. 1(d). The nodal lines have the open geometry. The protection is due to the non-symmorphic glide mirror plane $\mathcal{G}_x$ symmetry. Instead of assigning the $\mathcal{G}_x$ eigenvalues in the complex *ab initio* band structure, we verify this by excluding all other relevant symmetries as the origin of the protection. For $\mathbf{n}\ \|[100]$, the space group $P4/nmm$ of the tetragonal CuMnAs lattice reduces to eight symmetry elements: Identity, non-symmorphic glide planes $\mathcal{G}_x$, and $\mathcal{G}_z = \{M_z|\frac{1}{2}\frac{1}{2}0\}$, screw-axis $\mathcal{S}_y$=$\{C_{2y}|0\frac{1}{2}0\}$, and four $\mathcal{PT}$ conjugated symmetries. By rotating the Néel vector to $\mathbf{n}\|[110]$ and $\mathbf{n}\|[101]$, $\mathcal{G}_z$ and $\mathcal{S}_y$ remain symmetries of the AF crystal, respectively. In both cases, however, the nodal lines become gapped, as illustrated in Fig. 1(e), excluding the protection by these symmetries. Note that the $\mathcal{G}_x$ protection makes our tetragonal CuMnAs AF distinct from the earlier identified non-symmorphic protection in paramagnetic ZrSiS [6].

The field-like Néel SOT in the full tetragonal crystal of CuMnAs allows for the current-induced rotation of the Néel vector [7]. This opens the prospect of electric control of Dirac crossings in an

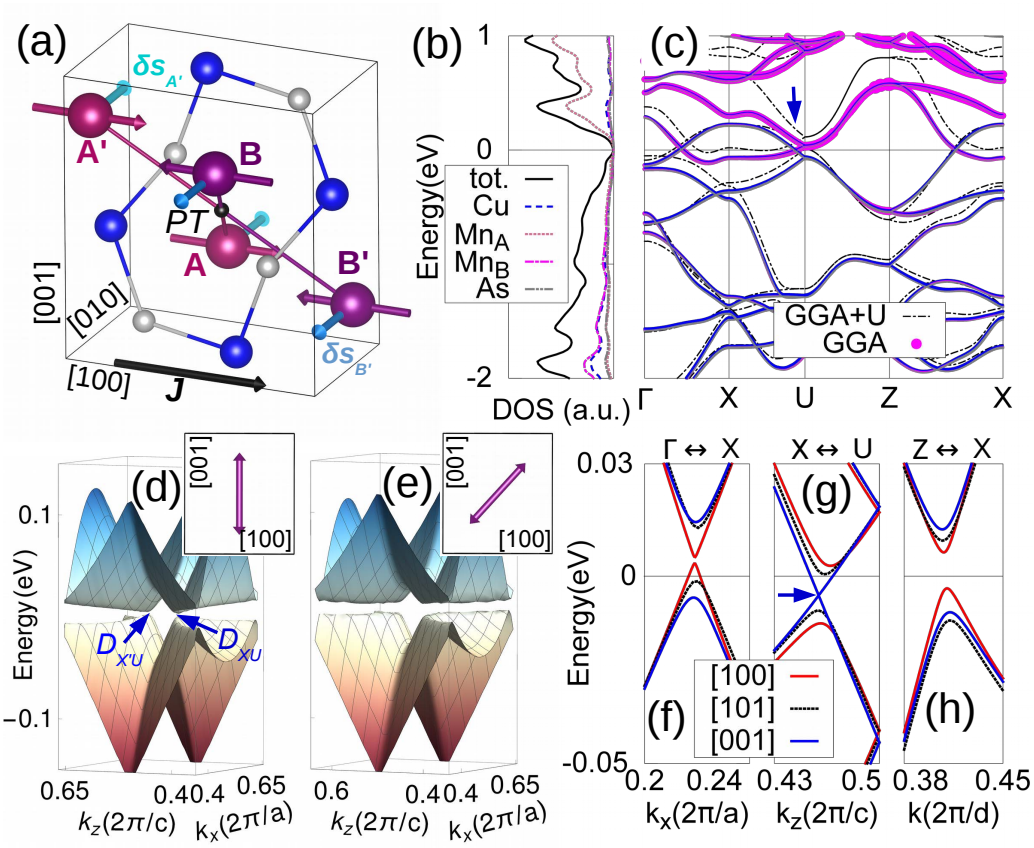

Figure 2: (a) Crystallographic and magnetic structure of the orthorhombic CuMnAs with Néel SOT spin-polarization $\delta\mathbf{s}$ for the current $\mathbf{J}\|[100]$. Atom-resolved (b) point-semimetal density of states, and (c) band structure without SOC within GGA. GGA+U shows DPs position shifts. (d-e) Topological MIT. Manipulation of the Dirac fermions along the (f) ΓX, (g) XU, and (h) ZX axis (units $d = \sqrt{a^2 + c^2}$ with $a \neq c$ being the lattice constants) by the Néel SOT from GGA+SOC calculations reveals: topological ($\mathbf{n}\|[001]$), and "trivial" Dirac semimetal ($\mathbf{n}\|[100]$), and semiconductor ($\mathbf{n}\|[101]$).

experimentally relevant AF material. However, the tetragonal CuMnAs is not optimal for observing the corresponding topological metal-insulator transition (MIT) due to other non-Dirac bands present around the Fermi level (see Fig. 1(c)). These can be removed, e.g., by lowering the lattice symmetry from tetragonal to orthorhombic, as we discuss below.

The non-symmorphic *Pnma* primitive cell of the orthorhombic CuMnAs is shown in Fig. 2(a). It has four Mn sites consisting of the two inversion-partner pairs A-B and A'-B'. From the symmetry analysis of the current-induced spin-polarizations generated locally at these four sites we obtain that they contain components which are commensurate with the AF order: A and A' sites with one sign of the current-induced spin-polarizations belong to one AF spin-sublattice and B and B' sites with the opposite sign of the current-induced spin-polarizations belong to the opposite AF spin-sublattice. This makes the Néel SOT efficient for reorienting AF moments in orthorhombic CuMnAs.

GGA electronic structure calculations without SOC are shown in Fig. 2(b),(c). The density of states vanishes at the Fermi level and we now discuss the properties of the three Fermi level Dirac points (DPs) seen in Fig 2(b),(c). Without SOC they are part of an ungapped nodal line in the $k_y = 0$ plane [8]. In the presence of SOC and for $\mathbf{n}\|$ [001], the DPs along the ΓX and ZX axes become gapped. The gap opening applies to the entire nodal line, except for the DP along the XU axis (and also X′U), as shown in Figs. 2(d),(f)-(h). Using the same method as in the *ab initio* calculations for the tetragonal CuMnAs, we identified that the XU DP protection is due to the screw-axis symmetry $S_z = \{C_{2z}|\frac{1}{2}0\frac{1}{2}\}$ [8]. The corresponding state at $\mathbf{n}\|[001]$ is then a topological AF Dirac semimetal

with the positive topological charge of the XU DP. For $\mathbf{n}\|[101]$, all DPs (the entire nodal line) are gapped and the system becomes an AF semiconductor, as seen in Figs. 4(e)-(h). Finally, for $\mathbf{n}\|[100]$, the spin-orbit gap is nearly but not fully closed at the ΓX DP, as shown in Fig. 2(f). This "trivial" AF Dirac semimetal phase is reminiscent of graphene. Our calculations predict a relatively weak magnetic anisotropy with the equilibrium easy axis along the [100]-direction. Note that the easy-axis determination with $E_{[001]} - E_{[100]} \sim 0.3$ meV per unit cell is at the resolution limit of our computational method. Since the DPs can appear at the Fermi level (see also the comparison of GGA and GGA+U calculations in Fig. 2(b)), orthorhombic CuMnAs represents a realistic material candidate for observing the topological MIT and AMR driven by the Néel vector reorientation.

1.2 Spectral function and resistivity anisotropy in Mn_2Au

In this work [2] we have elucidated the origin of the large anisotropic magnetoresostance observed in antiferromagnetic Mn_2Au by performing ab initio transport calculations and by inspecting anisotropies in the spectral function (see Fig. 3). A large contribution to the anisotropic magnetoresostance originates form opening and closing of a Dirac point near the Fermi level, as predicted in our above earlier theory work [1].

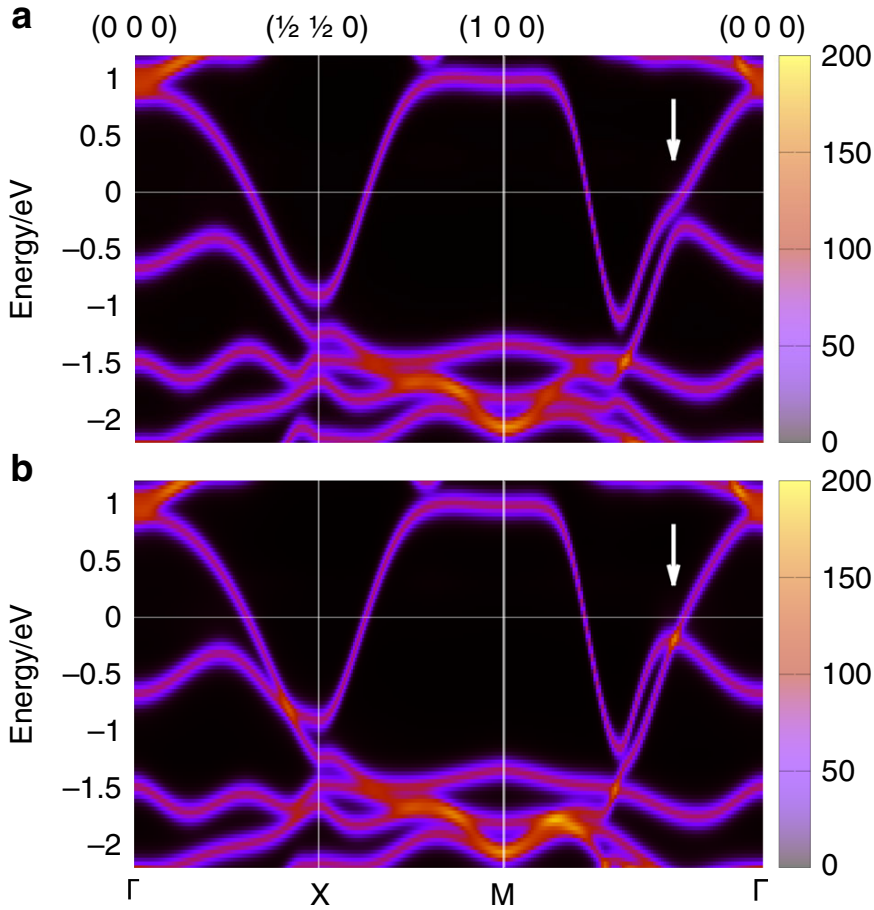

Figure 3: Bloch spectral function calculated in Mn2Au for two orthogonal orientations of the Néel vector; changes near the Dirac crossing are highlighted by arrows [2].

2 Magnetic Weyl semimetal without spin-orbit coupling and strong anomalous Hall effect in Ti2MnAl

In this work [9] we predict a magnetic Weyl semimetal in the inverse Heusler Ti2MnAl (see Fig. 4), a compensated ferrimagnet with a vanishing net magnetic moment and a Curie temperature of over 650 K. Despite the vanishing net magnetic moment, we calculate a large intrinsic anomalous Hall effect (AHE) of about 300 S/cm. It derives from the Berry curvature distribution of the Weyl points, which are only 14 meV away from the Fermi level and isolated from trivial bands. Different from antiferromagnets Mn3X (X = Ge, Sn, Ga, Ir, Rh, and Pt), where the AHE originates from the non-collinear magnetic structure, the AHE in Ti2MnAl stems directly from the Weyl points and is topologically protected. The large anomalous Hall conductivity (AHC) together with a low charge carrier concentration should give rise to a large anomalous Hall angle. In contrast to the Co-based ferromagnetic Heusler compounds, the Weyl nodes in Ti2MnAl do not derive from nodal lines due to the lack of mirror symmetries in the inverse Heusler structure. Since the magnetic structure breaks spin-rotation symmetry, the Weyl nodes are stable without spin-orbit coupling. Moreover, because of the large separation between Weyl points of opposite topological charge, the Fermi arcs extent up to 75% of the reciprocal lattice vectors in length. This makes Ti2MnAl an excellent candidate for the comprehensive study of magnetic Weyl semimetals. It is the first example of a material with Weyl points and large anomalous Hall effect despite a vanishing net magnetic moment.

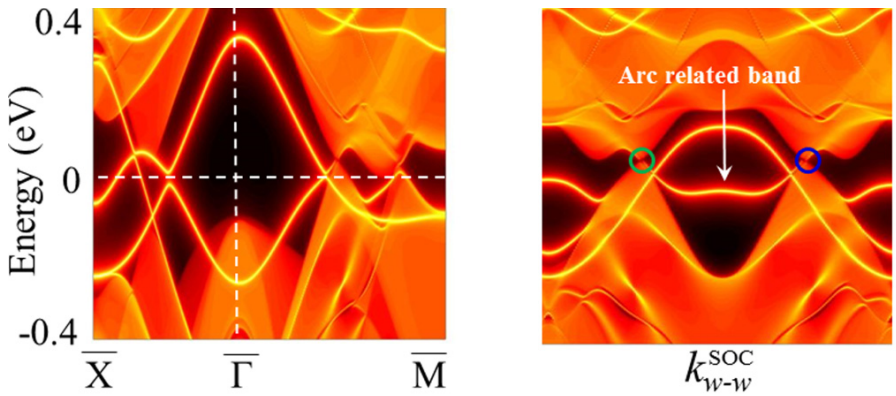

Figure 4: Surface energy dispersion of Ti2MnAl along high symmetry lines and crossing one pair of Weyl points [9].

3 Crystal time-reversal symmetry breaking and spontaneous Hall effect in collinear antiferromagnets

3.1 Overview

Previously, the spontaneous Hall effect has been understood in terms of the time-reversal symmetry breaking by the internal spin-structure of a ferromagnetic, non-colinear antiferromagnetic or skyrmionic form. In this work [10] we identify an overlooked robust Hall effect mechanism arising from collinear antiferromagnetism combined with non-magnetic atoms at non-centrosymmetric positions. We predict [10] and experimentally verify [11] a large magnitude of this crystal Hall effect in a room-temperature collinear antiferromagnet RuO_2 and catalogue, based on symmetry rules, extensive families of material candidates. We show that the crystal Hall effect is accompanied by the possibility to control its sign by the crystal chirality. We illustrate that accounting for the full magnetization density distribution instead of the simplified spin-structure sheds new light on symmetry breaking phenomena in complex magnets and opens an alternative avenue towards quantum materials engineering for low-dissipation nanoelectronics.

The spontaneous Hall voltage arises when the electrons gain transverse velocity due to certain internal magnetic structures. The associated Hall conductivity is the antisymmetric dissipationless part of the conductivity tensor, which corresponds to the Hall pseudovector $\boldsymbol{\sigma}$ that determines the Hall current [12, 13]:

$$\mathbf{j}_{\mathrm{H}} = \boldsymbol{\sigma} \times \mathbf{E}. \tag{1}$$

Here $\mathbf{E}$ is the applied electric field, $\boldsymbol{\sigma} = (\sigma_{zy}, \sigma_{xz}, \sigma_{yx})$, σ_{ij} are the antisymmetric Hall conductivity components, and $\mathbf{j}_{\mathrm{H}}$ is the Hall current transverse to $\mathbf{E}$ and $\boldsymbol{\sigma}$. Apart from being odd under time-reversal ($\mathcal{T}$), Eq. (1) explicitly highlights that the Hall effect transforms like a pseudovector under spatial symmetry operations, i.e., it transforms like a magnetic dipole moment. This implies that the *spontaneous* Hall effect (in the absence of an external field) can occur only in materials with a magnetic space group (MSG) in which a net magnetic moment is allowed by symmetry [14, 12, 15, 16, 17]. In fact, since the linear-response $\boldsymbol{\sigma}$ is invariant under the spatial inversion ($\mathcal{P}$), its components allowed by symmetry can be determined from the magnetic Laue group (MLG) [14, 12, 15]. In this work [10], we go beyond the mere MLG symmetry requirements on the spontaneous Hall effect by focusing on its microscopic physical mechanisms and chemistry of favourable material candidates, on the magnitude and means to control and detect the effect, and on links to the electronic structure topology.

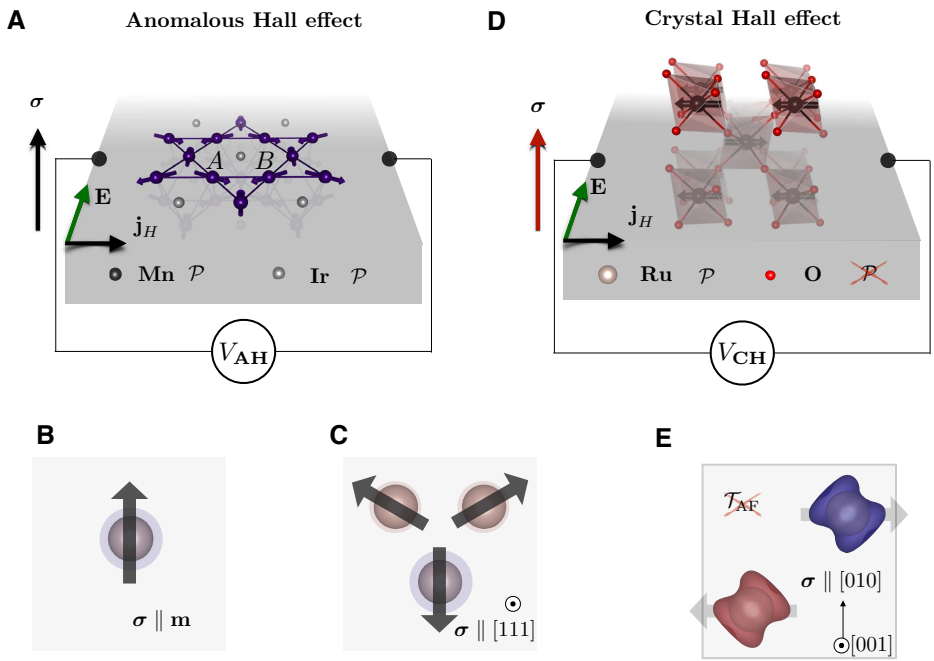

Figure 5: **Anomalous vs crystal Hall effect and corresponding magnetization isosurfaces.** (**A**) Anomalous Hall effect due to a Hall vector ($\boldsymbol{\sigma}$) generated by the non-collinear antiferromagnetic order (purple arrows) in Mn_3Ir (Mn: dark spheres, Ir: grey spheres). Mn and Ir atoms occupy centrosymmetric sites. The conventional symmetry breaking mechanism in anomalous Hall effect in ferromagnets (**B**) (**m** marks the magnetization vector) or non-collinear antiferromagnets (**C**) can be captured by the spin structure of the magnetic ions only (black arrows). (**D**) Crystal Hall effect generated by collinear antiferromagnetism (black arrows) and arrangement of non-magnetic atoms. (Ru: light brown spheres, O: red spheres). While the crystal has inversion centre at the magnetic Ru atom, the non-magnetic O atoms are at non-centrosymmetric positions. (**E**) In the case of the crystal Hall antiferromagnet, the complete magnetization density shape is required to capture the spontaneous symmetry breaking. In panels (B, C, E) we illustrate magnetisation density isosurfaces with projection along the [100] direction.

In the conventional microscopic mechanism of the spontaneous Hall effect in ferromagnets, the asymmetry of left-right deflected electrons is induced by the combined effect of ferromagnetic spin-polarization and spin-orbit coupling (SOC) [12]. This mechanism is commonly referred to as the anomalous Hall effect (AHE). Here the ferromagnetic polarization breaks the $\mathcal{T}$ symmetry, while SOC adds breaking of the invariance under spin rotation which, if the invariance was present, would make the AHE vanish as the invariance under $\mathcal{T}$ [16]. This required symmetry breaking and associated emergent magnetic Berry curvature can arise also due to certain non-collinear antiferromagnetic structures instead of ferromagnetic moments, as predicted for Mn_3Ir [18, 19] whose magnetic lattice is shown in Fig. 5A. Large AHE conductivities were experimentally reported in related coplanar non-collinear compensated antiferromagnets Mn_3Sn [20], Mn_3Ge [21], and Mn_3Pt [22]. The non-relativistic AHE counterpart - the topological Hall effect can occur when in the breaking of the spin-rotation invariance the SOC is replaced by a non-coplanar spin structure as shown in certain spin-liquid candidates [23], non-coplanar antiferromagnets [24], or skyrmions [25].

The formal MLG symmetry analysis of the spontaneous Hall effect has not led, over the five decades since its original report [14], to the identification of a suitable material candidate with collinear antiferromagnetic order. Focusing on the spin vectors and spatial configurations of magnetic atoms [16], as illustrated in Figs. 5B,C, has even resulted in a general expectation of a vanishing spontaneous Hall effect in collinear antiferromagnets [24, 26, 16, 27]. Indeed, antiferromagnets with $\mathcal{T}$ symmetry in the MLG are excluded from having the spontaneous Hall effect. Examples encompass collinear antiferromagnets that have a symmetry termed here $\mathcal{T}_{\mathrm{AF}}$ combining $\mathcal{T}$ and another symmetry operation, as for instance CuMnAs [1] ($\mathcal{T}_{\mathrm{AF}} = \mathcal{P}\mathcal{T}$), or GdPtBi [28] ($\mathcal{T}_{\mathrm{AF}} = \mathbf{t}_{\frac{1}{2}}\mathcal{T}$, where $\mathbf{t}_{\frac{1}{2}}$ is a half-unit cell translation).

The breaking of the $\mathcal{T}$ symmetry in the MLG by the spin structure of ferromagnets or the non-collinear magnetic systems has been at the heart of all the above Hall effect considerations. In this work [10], we introduce an alternative relativistic spontaneous Hall mechanism. Here the simplified magnetic structure alone, represented by the spin vectors and spatial configurations of magnetic atoms, generates no spontaneous Hall conductivity. The required asymmetry is generated only when including additional atoms at non-centrosymmetric sites which can be non-magnetic. Our mechanism is demonstrated on the collinear antiferromagnet RuO_2 shown in Fig. 5D. Here the crystal arrangement of oxygen atoms results in the asymmetry of magnetization density on the opposite Ru spin-sublattices, as illustrated in Fig. 5E, which breaks $\mathcal{T}_{\mathrm{AF}}$. This shows that while the symmetry breaking mechanism in ferromagnets or non-collinear antiferromagnets can be captured by drawing magnetic ordering as spin-projection vectors only, placed on the magnetic atom sites (Figs. 5B,C), this common approach is incomplete in general. On the example of a collinear antiferromagnetic order, we illustrate that the detailed shape of the magnetization density needs to be considered, otherwise important families of magnets are omitted.

A specific consequence of our crystal symmetry breaking mechanism in the context of the spontaneous Hall effect is flipping off the sign of the Hall coefficient when reversing the crystal chirality by the rearrangement of the non-magnetic atoms while keeping the spin vectors and the positions of magnetic atoms fixed. The crystal chirality thus offers an additional tool, apart from reversing the magnetic moments, to control the sign of the Hall effect which is not available in the earlier identified anomalous Hall effects of ferromagnets or non-collinear antiferromagnets. To highlight the unique nature and consequences of our mechanism we introduce the term crystal Hall effect (CHE). On the example of the collinear antiferromagnet RuO_2 we also illustrate that the crystal symmetry breaking mechanism is robust, leading to large magnitudes of the CHE.

While RuO_2 has oxygen atoms on locally non-centrosymmetric sites, it is globally centrosymmetric. We analyse also the CHE in the quasi-two-dimensional antiferromagnet [27] $CoNb_3S_6$ which is globally non-centrosymmetric. We catalogue all possible magnetic symmetries hosting the CHE in collinear antiferromagnets and a number of material candidates. Finally, we discuss the relevance of the CHE for earlier inconclusive interpretations of Hall measurements [27, 29] in the above mentioned $CoNb_3S_6$ and in the Ce-doped canted antiferromagnet $CaMnO_3$.

3.2 Crystal symmetry breaking mechanism in a collinear antiferromagnet

We now describe the $\mathcal{T}$ symmetry breaking due to the complex asymmetric magnetization density in collinear antiferromagnets, emphasizing the distinct nature of the CHE from the usual AHE mechanism. The anomalous Hall conductivity in $IrMn_3$ and similar materials is generated by the symmetry lowering due to the *nontrivial* non-collinear antiferromagnetic order [16]. The magnetization densities are locally highly symmetric as illustrated in Fig. 5C, and the $\mathcal{T}$ symmetry is broken in the MLG by the mutual non-collinearity of the spin-projection vectors on the magnetic sites. The Fermi surfaces exhibit non-collinear spin textures in the crystal momentum space and spin is not a good quantum number even without SOC. Ir Wyckoff positions are centrosymmetric and the MSG does not depend on their presence or absence in the $IrMn_3$ crystal. This justifies neglecting the non-magnetic atoms in this class of crystals and analysing only the magnetic spin-structure [16]. The SOC lifts the degeneracy between two magnetic states connected by spin reversals and translates the symmetry breaking into the orbital sector, similarly as in the ferromagnetic AHE [16].

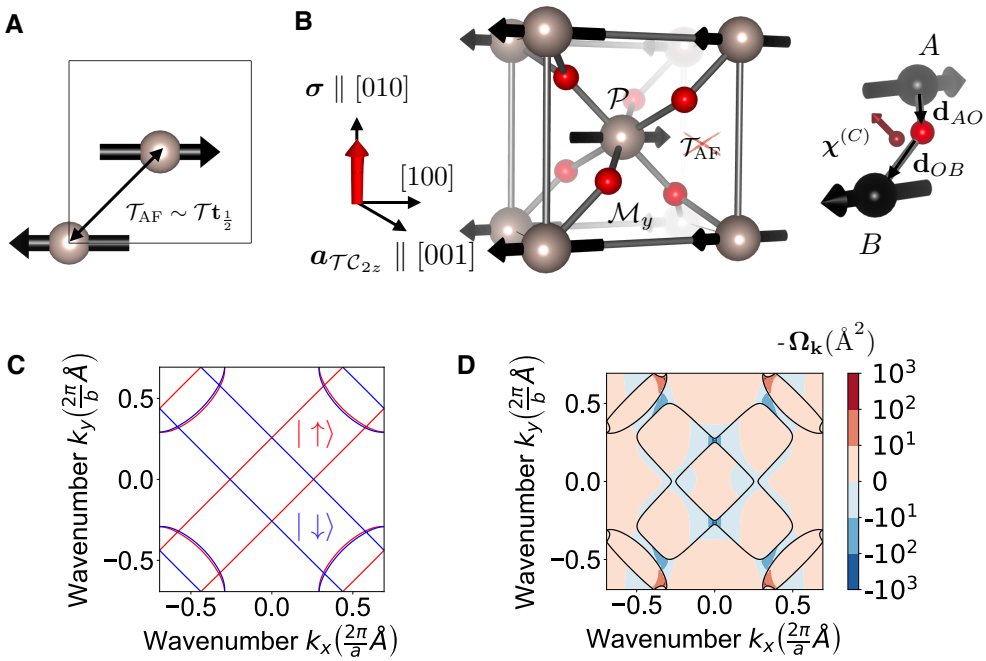

Figure 6: **Crystal symmetry breaking, large spin split Fermi surface, and Berry curvature in collinear antiferromagnet RuO_2.** (**A**) Collinear antiferromagnet with effective time-reversal symmetry $\mathcal{T}\mathbf{t}_{\frac{1}{2}}$. (**B**) Left: the unit cell of antiferromagnetic RuO_2 with the Néel vector along the [100]-axis and marked crystal symmetries. Right: detail of the generation of the local crystal chirality by non-centrosymmetric oxygen atoms $\boldsymbol{\chi}^{(C)}_{AB} \sim \mathbf{d}_{AO} \times \mathbf{d}_{OB}$. (**C**) Antiferromagnetic Fermi surface cut at wavevector $k_z = 0$ calculated without spin-orbit coupling. The spin up and down projections are coloured in red and blue. (**D**) Calculations with spin-orbit coupling of crystal momentum resolved Berry curvature $\Omega_y(k_x, k_y, 0)$ in atomic units.

From this perspective, the two-site collinear antiferromagnet, as shown in Fig. 6A, is trivial since it cannot generate any Hall signal due to the $\mathcal{T}_{\mathrm{AF}}$ symmetry. However, by interlacing the magnetic lattice by the non-magnetic atoms distributed at non-centrosymmetric positions, we can break the $\mathcal{T}_{\mathrm{AF}}$ symmetry, as we show in Figs. 5D,E and in Fig. 6B on the rutile antiferromagnet RuO_2. For the collinear antiferromagnetism with quantization axis along the [100] direction, the system acquires MSG $Pn'n'm$ (Type-III), magnetic point group (MPG) $m'm'm$, and MLG $2'2'2$. The symmetry

generators are $\mathcal{P}$, glide mirror plane $\mathcal{M}_y\mathbf{t}$ ($\mathbf{t} = (\frac{a}{2}, \frac{a}{2}, \frac{c}{2})$) marked in Fig. 6B, and antiunitary rotation $\mathcal{TC}_{2z}$ and they do not change when we cant the perfectly antiparallel magnetic moments towards the [010] direction. This illustrates the ferromagnetic nature of the symmetry groups even in a fully compensated antiferromagnetic state with the Hall vector $\boldsymbol{\sigma} = (0, \sigma_{xz}, 0)$.

In Figs. 6C,D we illustrate the microscopic mechanism which generates a non-zero Berry curvature with collinear antiferromagnetism. In the non-magnetic state, the bands are Kramers degenerate due to the $\mathcal{P}$ and $\mathcal{T}$ symmetries [1] of the rutile crystal. When we introduce the collinear antiferromagnetic order, the distribution of oxygen atoms deforms the magnetization densities around the Ru sublattices, as we show in Fig. 5E. The magnetization density explicitly illustrates breaking of the $\mathcal{T}_{\mathrm{AF}}$ symmetry for a generic crystal momentum $\mathbf{k}$. However, the effective symmetry comprising of rotating the magnetization densities (oxygen octahedra) by 90 degrees around each Ru atom in combination with half-unit cell translation enforces the two Ru atoms to be in the antiferromagnetic spin state. In turn, the integrated even-in-magnetization quantities such as the density of states (DOS) when SOC is switched-off remain perfectly compensated.

Remarkably, the energy bands are strongly spin-split for a generic $\mathbf{k}$, even when the relativistic SOC is switched-off in the density functional theory (DFT) calculation – see red/blue-coloured bands in Fig. 6C. In contrast to the non-collinear antiferromagnets, spin is a good quantum number here in the absence of SOC. When the relativistic corrections are switched on, the local non-cetrosymmetricity also generates ASOC $\sim \mathbf{k} \times \nabla V \cdot \mathbf{s}$, which additionally lowers the symmetry. The resulting band structure is locally spin-polarized, spin mixed, and generates the required asymmetry between left and right moving electrons as can be seen on large Berry curvature hotspots around the additional spin-splittings in Fermi surface bands shown in Fig. 6D. Note that the net moment generated by the Dzyaloshinskii-Moriya interaction (DMI) is known to be a relativistic effect of a small magnitude [30]. In contrast, our calculations demonstrate that the spin-symmetry breaking is not a small correction but a strong effect reflected in large magnitudes of the CHE.

We calculate the intrinsic Hall conductivity (independent of disorder-scattering) by integrating the Berry curvature, $\boldsymbol{\Omega}(\mathbf{k}) = -\mathrm{Im}\langle\partial_{\mathbf{k}}u(\mathbf{k})| \times |\partial_{\mathbf{k}}u(\mathbf{k})\rangle$, in the crystal momentum space (see Methods). In Fig. S3 we show that the non-vanishing integral component $\int dk_x \Omega_y(\mathbf{k})$ is even in k_y as we expect from the symmetry analysis, while the $\mathcal{M}_y$, $\mathcal{P}$ and $\mathcal{TC}_{2z}$ symmetries imply that $\int dk_x \Omega_x(\mathbf{k}) = 0$, and $\mathcal{M}_y$, and $\mathcal{TC}_{2z}\mathcal{M}_y$ yield $\int dk_z \Omega_z(\mathbf{k}) = 0$. We obtain $\sigma_{xz} = 35.7$ Scm^{-1}, demonstrating a large crystal Hall conductivity in stoichiometric RuO_2. The DFT calculations of the CHE are extensively discussed below.

3.3 Crystal chirality control of the Hall conductivity

We now demonstrate the possibility to control the Hall conductivity sign by swapping the crystal chirality. In Figs. 7A, B we show the RuO_2 crystal with the two possible distributions of the oxygen atoms corresponding to the opposite crystal chiralities $\boldsymbol{\chi}^{(C)} = \pm 1$. While the MSG is the same in both cases, the local magnetization densities, obtained from the DFT calculations, are rotated by 90 degrees [31]. In Fig. 7C we plot the energy bands corresponding to the crystal in Fig. 7A. The red and blue arrows mark spin up and down projection for the bands calculated without SOC. When we include the SOC we obtain additional splittings of the bands and large Berry curvature, as we show in Figs. 6D and 7D. The red and blue colours correspond to the opposite local chirality crystals shown in Figs. 7A, B.

The flipping of the sign of CHE σ_{xz} with the Néel vector reversal is consistent with the Onsager relations. The two crystals in Figs. 7A, B can be mapped on each other by the $\mathcal{T}$ operation combined with a half-unit cell translation and this symmetry ensures the same magnitude, while opposite sign, of σ_{xz} for the two crystal chiralities.

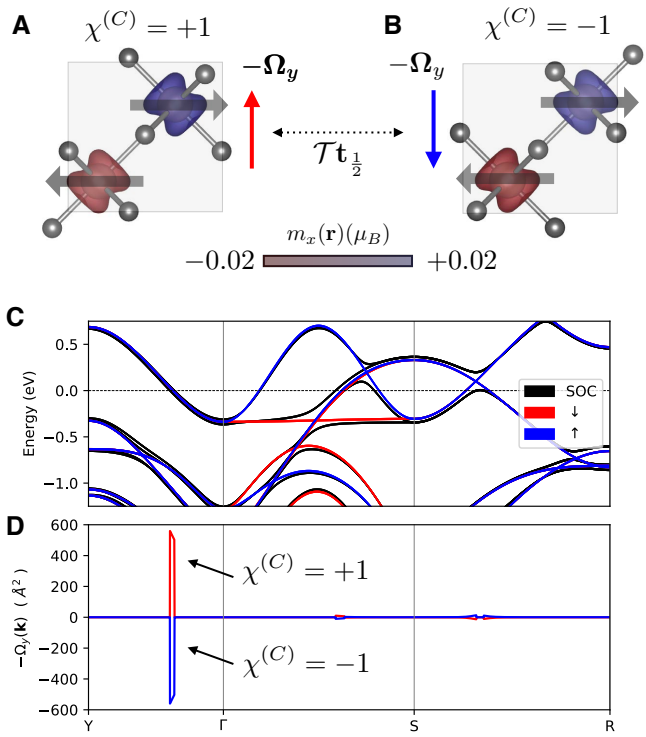

Figure 7: **Crystal chirality control of Hall conductivity sign.** (**A**), (**B**) View along the tetragonal crystal axis on the RuO_2 crystal with two possible configurations of non-magnetic oxygen atoms. Redistribution of the oxygen atoms does not change the magnetic symmetry of the crystal, however, it changes the local crystal chirality orientation $\boldsymbol{\chi}^{(C)}$ and rotates by 90° the shape of the magnetization density isosurfaces. (**C**) Calculated energy bands in the RuO_2 antiferromagnet without spin-orbit coupling (red and blue bands correspond to the opposite spin-projections), and with spin-orbit coupling (black bands). (**D**) The largest contribution to the Berry curvature $\mathbf{\Omega}$ originates from the spin-split bands by the spin-orbit coupling. The red and blue colour corresponds to the two opposite crystal chiralities $\boldsymbol{\chi}^{(C)}$ and demonstrates the expected Berry curvature sign change (compare to panels (A) and (B)).

3.4 Crystal Hall phenomenology in RuO_2, $CoNb_3S_6$, and other collinear antiferromagnets

In Fig. 8A we identify a sizable CHE conductivity in the room temperature collinear antiferromagnet RuO_2 by our first-principle calculations. Note that among the rutile antiferromagnets, a metallic phase is rare which makes the recently discovered [32, 33] itinerant antiferromagnetism in RuO_2 exceptional within this family of simple collinear antiferromagnets. Our DFT calculations show that for a medium strength Hubbard parameter ($U \sim 1-3$ eV), antiferromagnetism and metallic density of states (DOS) coexist, consistent with previous reports [32, 33]. We set in all plots in the main text $U \sim 2$ eV, which reproduces best the experimental antiferromagnetic moments.

When turning the sizable SOC off in our DFT calculation, we observe a perfect antiferromagnetic compensation in the Ru-projected DOS. With the large atomic SOC turned on, only minute corrections to the DOS occur, as shown in Fig. 8B. They result in a small net magnetic moment, $\mathbf{m} = \mathbf{m}_A + \mathbf{m}_B$, of a magnitude ~ 0.05 μ_B due to the DMI [30]. Here $\mathbf{m}_{A/B}$ are magnetizations of the antiferromagnetic A and B sublattices. In comparison, the Néel vector $\mathbf{n} = (\mathbf{m}_A - \mathbf{m}_B)/2$ has a magnitude ~ 1.17 μ_B.

To gain further insight, we calculate the dependence of the CHE for $\mathbf{n} \parallel [100]$ on the canting angle between magnetizations of sublattices A and B, see Fig. 8A. Furthermore, we separate in Fig. 8A σ_{xz}

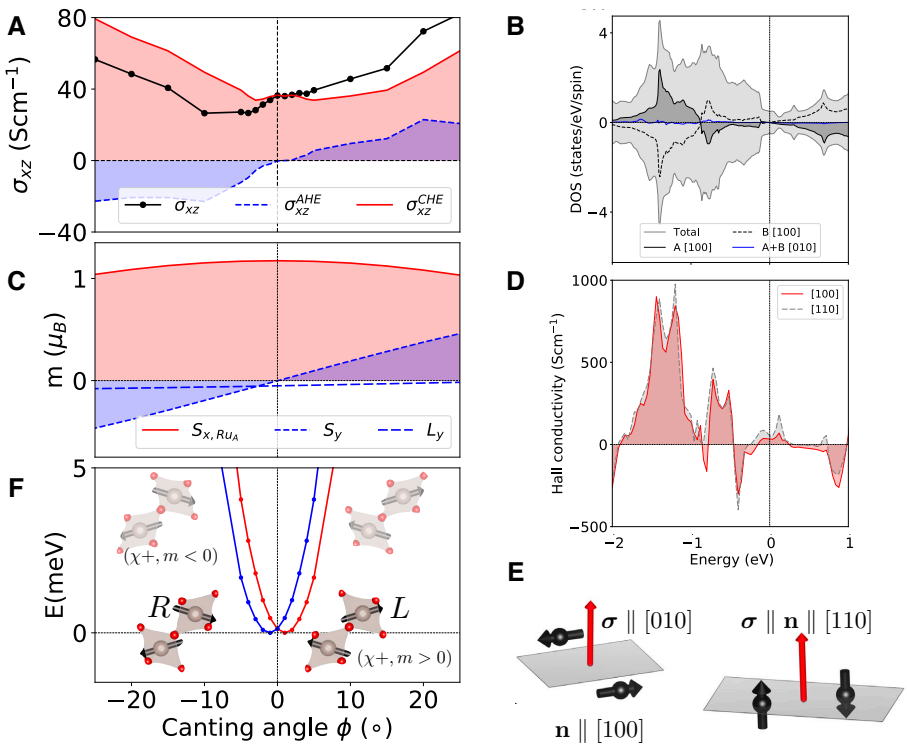

Figure 8: **First-principle calculation of sizeable and anisotropic crystal Hall effect in RuO_2.** (**A**) First-principle calculation of the dependence on the canting angle of the Hall conductivity and its separation into the anomalous (ferromagnetic) and crystal (antiferromagnetic) parts. (**B**) Ru sublattice A (solid) and B (dashed) projected DOSs for the Néel vector along the [100] axis. Black solid and dotted lines show calculations with spin-orbit coupling of the DOS component for moments projected along the [100] axis. Blue line shows the sum of sublattice DOSs for the moment projection along the [010] axis which corresponds to the small canting of the antiparallel moments due to Dzyaloshinskii-Moriya interaction. (**C**) The dependence on the canting angle of the spin component S_x (projected on single Ru sublattice A), S_y (total net spin moment) and orbital magnetization L_y. (**D**) Energy dependence of the calculated crystal Hall conductivity for $\mathbf{n} \parallel [100]$ (red solid line) and $\mathbf{n} \parallel [110]$ (gray dashed line). (**E**) The mutual orientation of the Néel vector $\mathbf{n}$, and Hall vector $\boldsymbol{\sigma}$. (**F**) Two magnetic domains with opposite Néel vector induced by opposite field H and the corresponding energy costs for canting. $\mathbf{H} \parallel [010]$ corresponds to canting angles $\phi > 0$ and prefers $\mathbf{n} \parallel [100]$ (red) over $\mathbf{n} \parallel [\bar{1}00]$ (blue). In the inset we depict four combinations of the local crystal chirality and Néel vector orientations. The two combinations marked L and R have the lowest energy.

into a contribution even in $\mathbf{m}$:

$$\sigma_{xz}^{\mathrm{CHE}} = [\sigma_{xz}(\mathbf{n}, \mathbf{m}) + \sigma_{xz}(\mathbf{n}, -\mathbf{m})]/2, \tag{2}$$

and odd in $\mathbf{m}$:

$$\sigma_{xz}^{\mathrm{AHE}} = [\sigma_{xz}(\mathbf{n}, \mathbf{m}) - \sigma_{xz}(\mathbf{n}, -\mathbf{m})]/2. \tag{3}$$

Here $\sigma_{xz}^{\mathrm{AHE}}$ corresponds to a contribution induced by the small net moment, analogous to the AHE in ferromagnets. We see that this term is roughly linear in $\mathbf{m}$ (see Figs. 8A and 8C), at least for $|\phi| \lesssim 10°$, while $\sigma_{xz}^{\mathrm{CHE}}$ is almost constant at small ϕ and dominates the contribution to σ_{xz}. Hence the small net magnetic moment has a negligible effect on σ_{xz}. This is in striking contrast to the recently studied antiferromagnets GdPtBi [28] and $EuTiO_3$ [34], which order in a $\mathcal{T}$-invariant MLG and whose observed AHE is entirely due to the canting induced by an applied external magnetic field.

In Fig. 8D we plot the intrinsic crystal Hall conductivity for the Néel vector orientation along [100] and [110] crystal axies as a function of the Fermi level position which simulates, e.g., off-stoichiometry

or alloying with other elements. For artificially constrained perfectly antiparallel spin moments along the [100] axis, $\boldsymbol{\sigma} \parallel [010]$ and we obtain $\sigma_{xz} = 36.4$ Scm^{-1} for stoichiometric RuO_2. For a canting angle $\approx 1^\circ$ obtained from the DFT calculation, $\mathbf{m} \parallel [010]$ and $\sigma_{xz} = 35.7$ Scm^{-1}. For the Néel vector along the [110] axis, $\sigma_H = 54.6$ Scm^{-1}. These crystal Hall conductivities are comparable to the large anomalous Hall conductivities in non-collinear antiferromagnets Mn_3Sn (100 Scm^{-1} in experiment[20] and 133 Scm^{-1} in theory[35]) or Mn_3Pt (74 Scm^{-1} in experiment and 57 Scm^{-1} in theory [22]), and are much larger than the topological Hall conductivities in antiferromagnetic spin liquid candidates (<5 Scm^{-1} [23]). For Fermi level shifts of ≈ -0.5 eV, corresponding to a reduced filling by one electron in off-stoichiometric $Ru_{1+x}O_{2-x}$, the CHE conductivity can be as large as ~ 300 Scm^{-1}. At larger energy shifts (≈ -1 eV) even ~ 1000 Scm^{-1} is reached. This is similar to the record magnitudes reported for the AHE in ferromagnets or non-collinear antiferromagnets [12, 21].

The CHE can also show a large anisotropy in the Hall conductivity which can be understood in terms of the symmetry imposed dependence of the hybridization of linear band crossings and of the gapping of nodal-line features [36] on the Néel vector orientation [1]. For example, the MSG changes from $Pnn'm'$ for $\mathbf{n} \parallel [100]$ to $Cnn'm'$ for $\mathbf{n} \parallel [110]$.

We observe that DMI generates a small magnetization that is perpendicular to the Néel vector when $\mathbf{n} \parallel [100]$ while, for $\mathbf{n} \parallel [110]$, it generates a small parallel magnetization. While in the former case the Hall vector is perpendicular to the Néel vector, in the latter case the two vectors are parallel as we schematically illustrate in Fig. 8E. Also, from Figs. 8A, C we see that the crystal Hall conductivity is proportional to neither spin nor orbital magnetization and, for a generic angle of the Néel vector, the mutual orientation of the Néel and Hall vectors is arbitrary and depends on microscopic details.

The sign of the Hall conductivity can be controlled also by the global crystal chirality. We explain this on the $CoNb_3S_6$ crystal (its low-symmetry magnetization isosurfaces are shown in Fig. 9A), a quasi-2d hexagonal collinear antiferromagnet derived from the Van der Waals crystal of transition metal dichalcogenide NbS_2 [27]. The opposite sign of crystal Hall conductivity, shown in Figs. 9B, C, corresponds to the two crystals with the opposite sense of the spatial inversion symmetry breaking, marked L and R in Fig. 9B.

$CoNb_3S_6$, with collinear antiferromagnetic moments, has the $C2'2'2_1$ MSG and the same MLG as RuO_2 ($2'2'2$), where the unprimed rotational axis $\mathcal{C}_2$ is perpendicular to the hexagonal layers and $\boldsymbol{\sigma} \parallel \mathbf{a}_{\mathcal{C}_2}$ (according to our classification in Tab. 1). However, the global $\mathcal{P}$ symmetry breaking promotes the role of ASOC, as we show in Fig. 9D, where the bands are split along the high symmetry axes, not only at high symmetry points. The energy bands, e.g. around the H point, are substantially split by the ASOC and in combination with collinear antiferromagnetism, a large Berry curvature Ω_z is generated as we illustrate on the Berry curvature summed up to the lowest energy band shown in Fig. 9D. The Berry curvature appears to be concentrated around these antiferromagnetic generalisations of Kramers-Weyl-like dispersions [37].

We note that the spontaneous Hall effect recently detected in $CoNb_3S_6$ [27] could not be reconciled with a collinear antiferromagnetic order inferred from neutron scattering. Our first-principles calculations shown in Fig. 9C give a magnitude of the CHE in hole-doped (Fermi energy ~ -0.7 eV) $CoNb_3S_6$ which is consistent with the experimental value for this doping level- (27 S/cm [27]).

While the symmetry allowed direction of the Hall vector $\boldsymbol{\sigma}$ depends only on the MLG, the possibility to control the sign of the CHE by the local or global crystal chirality depends on the full MPG. To enumerate all possible symmetries allowing for the CHE in collinear antiferromagnets we start by excluding antiferromagnetic symmetries incompatible with the existence of a Hall vector. Among those are all MSG-type-IV antiferromagnets with $\mathcal{T}_{\rm AF} = \mathbf{t}_{\frac{1}{2}}\mathcal{T}$ symmetry ($\mathbf{t}_{\frac{1}{2}}$ is half-unit cell translation as e.g. in GdPtBi), and MSG-type-III antiferromagnets $\mathcal{T}_{\rm AF} = \mathcal{P}\mathcal{T}$ symmetry (e.g. CuMnAs, or Mn_2Au) which have the $\mathcal{T}$ symmetry in the MLG. In total, 275 MSGs, 31 MPGs, and 10 MLGs of type I and III remain as candidates for spontaneous Hall effects. However, simple collinear antiferromagnetism is not compatible with 3-fold, 4-fold, and 6-fold rotational symmetries. We summarize in Tab. 1 the remaining 12 MPGs and 4 MLGs that may host the CHE in collinear antiferromagnets.

We can formulate simple rules allowing for a fast determination of the orientation of the Hall vector

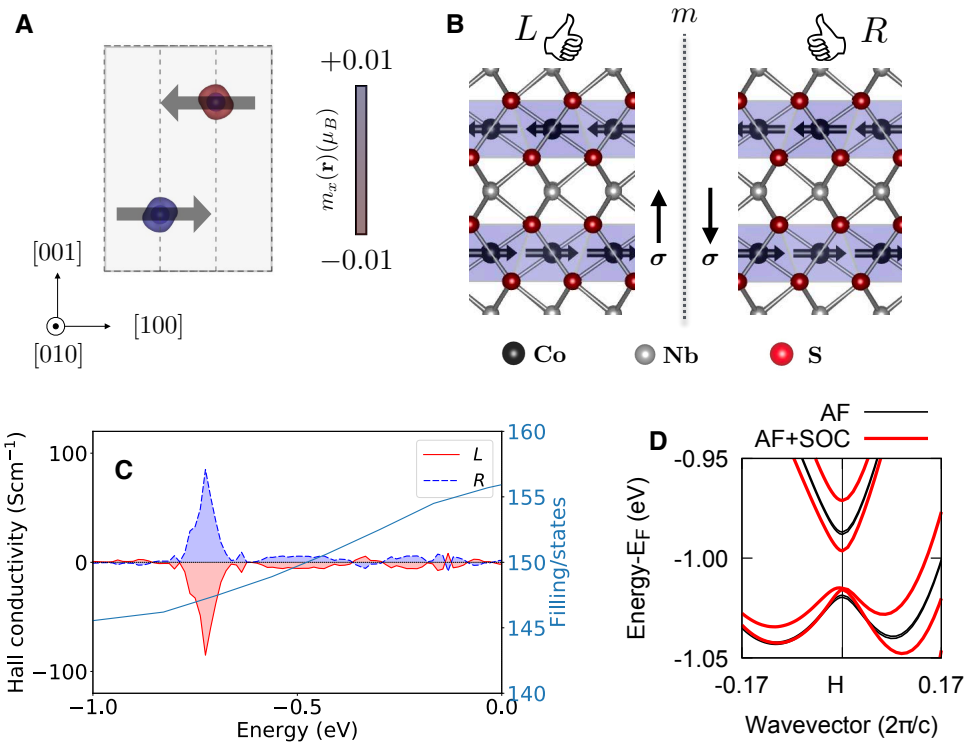

Figure 9: **Crystal Hall conductivity in the chiral crystal of $CoNb_3S_6$ antiferromagnet.** (**A**) Calculated magnetization isosurfaces in the $CoNb_3S_6$ antiferromagnet exhibit low symmetry and illustrate the global chiral symmetry breaking. (**B**) The crystal of the $CoNb_3S_6$ antiferromagnet ("L", with a left-handed chirality) and its mirror m image ("R", with a right-handed chirality). Note that the mirror m maps the two chiralities onto each other by redistributing the non-magnetic S atoms, while preserving the magnetic atom positions and orientations of the colllinear antiferromagnetic moments. (**C**) The calculated crystal Hall conductivity (left axis) changes sign when the crystal chirality is reversed from left- to right-handed. The right axis corresponds to the calculated dependence of the electron filling on energy. (**D**) Band structure detail of antiferromagnetic $CoNb_3S_6$ without (black line) and with (red line) spin-orbit coupling. We show fraction of the LHA path in Brillouin zone.

$\boldsymbol{\sigma}$ based on the existence of these only 4 MLGs. (i) In MLG 1 the orientation of $\boldsymbol{\sigma}$ is arbitrary and depends on microscopic details of the electronic structure. (ii) In systems with $2'$ rotational axis the Hall vector is perpendicular to the axis and the orientation within this plane is set microscopically. (iii) The 2 fold rotational axis constrains the Hall vector to be parallel to this axis (see Fig. 5A and 9B) and the orientation of the Hall vector is determined uniquely by the symmetry. All the remaining possibilities can be derived from these three cases (for instance in $2'2'2$ the Hall vector is perpendicular to both $2'$ and parallel to 2).

We point out that as many as $\sim 10\%$ of the total of ~ 700 magnetic structures reported in the Bilbao MagnData database [38] belong to the class of collinear antiferromagnets in which the CHE is allowed by symmetry. We point out that our CHE mechanism will materialize in these candidates possibly also in its optical or thermal variants. In Tab. 1 we list some additional material candidate examples such as orthoferrites, perovskites, or corundum structure materials.

The CHE might also contribute to Hall signals which were earlier taken as a signature of nontrivial and topological magnetization textures. This applies, e.g., to the measured spontaneous Hall signal in a Ce-doped canted antiferromagnet $CaMnO_3$ (MPG $2'/m'$) [29]. Apart from the AHE contribution due to the net magnetic moment, our symmetry analysis shows that the CHE associated with the Néel vector, rather than the canting moment (cf. Figs. 8A, C) is allowed in this material due to the oxygen non-centrosymmetric positions. The spikes arising in the Hall signal by applying a magnetic

field can be alternatively explained as a convolution of two spontaneous Hall signals from material regions with the opposite Hall sign [39]. These two regions might correspond to the two crystallites with the opposite sign of the CHE. Furthermore, methods for growing single-crystal-chirality systems can be used to enhance the Hall signal.

Finally, we remark that existing mechanisms of the quantum spontaneous Hall effect rely either on rare ferromagnetic insulators or on fragile diluted magnetic topological insulators with low critical temperatures and small magnetic band-gaps [40]. Our crystal spontaneous symmetry breaking represents a long-sought mechanism marrying strong Hall response with a robust room-temperature intrinsic collinear antiferromagnetism.

MLG	Centrosymmetric MPG	$\boldsymbol{\sigma}$	Non-centrosymmetric MPG	$\boldsymbol{\sigma}$	Material	Tensor
1	$\bar{1}$	arb.	1	arb.	Fe_2O_3	$\begin{pmatrix} \sigma_{xx} & \sigma_{xy} & \sigma_{xz} \\ \sigma_{yx} & \sigma_{yy} & \sigma_{yz} \\ \sigma_{xz} & \sigma_{zy} & \sigma_{zz} \end{pmatrix}$
2	$2/m$	$\parallel \mathbf{a}_{\mathcal{C}_2}$ $\perp \mathcal{M}$	2 $\parallel \mathbf{a}_{\mathcal{C}_2}$ / m $\perp \mathcal{M}$		$BiCrO_3$	$\begin{pmatrix} \sigma_{xx} & 0 & \sigma_{xz} \\ 0 & \sigma_{yy} & 0 \\ \sigma_{xz} & 0 & \sigma_{zz} \end{pmatrix}$
$2'$	$2'/m'$	$\perp \mathbf{a}_{\mathcal{TC}_2}$ $\in \mathcal{TM}$	$2'$ $\perp \mathbf{a}_{\mathcal{TC}_2}$ / m' $\in \mathcal{TM}$		$CaMnO_3$ [29]	$\begin{pmatrix} \sigma_{xx} & \sigma_{xy} & \sigma_{xz} \\ -\sigma_{xy} & \sigma_{yy} & \sigma_{yz} \\ -\sigma_{xz} & -\sigma_{yz} & \sigma_{zz} \end{pmatrix}$
$2'2'2$	$m'm'm$	$\parallel \mathbf{a}_{\mathcal{C}_2}$ $\perp \mathcal{M}_z$	$2'2'2$ $m'm'2$ $\parallel \mathbf{a}_{\mathcal{C}_2}$ / $m'm2'$ $\perp \mathcal{M}_y$		RuO_2 [33] $CoNb_3S_6$ [27]	$\begin{pmatrix} \sigma_{xx} & \sigma_{xy} & 0 \\ -\sigma_{xy} & \sigma_{yy} & 0 \\ 0 & 0 & \sigma_{zz} \end{pmatrix}$

Table 1: Catalogue of Hall-vector admissible magnetic point groups in collinear antiferromagnets and selected material candidates. First two rows list Type-I and last two rows Type-III magnetic point groups (MPGs), respectively. We list more material candidates and all magnetic symmetries allowing any Hall signal in SM Tab. S2. If not referenced otherwise, the material candidate was obtained from the MagnData database [38]. MLG marks the magnetic Laue group.

3.5 Experimental observation of the crystal Hall effect in RuO_2

To experimentally verify the crystal Hall effect, we used in this work [11] high-quality epitaxial thin films of RuO_2 on MgO single-crystal substrates. The Hall measurements conducted up to 50 T that was applied along the out-of-plane direction of thin film samples in a pulsed high magnetic field setup demonstrated a clear anomalous Hall effect at all temperatures ranging from 10 to 300 K. The Hall data are shown in Figs. 10A,B and exhibit an anomalous signal, i.e., the departure from ordinary Hall effect linear in magnetic field. This signal is consistent with the crystal Hall mechanism. Considering the saturation crystal Hall resistivity ρ_{CHE} and the transverse resistivity ρ (Fig. 10C) of the RuO_2 film at different temperatures, the magnitude of the anomalous Hall conductivity estimated from $|\sigma_{\mathrm{CHE}}| \approx \rho_{\mathrm{CHE}}/\rho^2$ is plotted as a function of temperature in Fig. 10D. Due to the highly metallic nature of the RuO_2 film, $|\sigma_{\mathrm{CHE}}|$ is rather large at low temperatures. It reaches 331 S/cm, which is over three times that of non-collinear antiferromagnet Mn_3Sn and even on the same order with the anomalous Hall conductivity of Fe thin films. Above 50 K, $|\sigma_{\mathrm{CHE}}|$ is greatly lowered by increasing temperature and decreases to ~ 3.2 S/cm at room temperature.

Compared with RuO_2 films grown on MgO, RuO2 films deposited onto $SrTiO_3$ single-crystal substrates in the same optimized conditions are highly ordered as well but (100)-oriented (Fig. 10E). Intriguingly, the Hall effect along the RuO_2[100] direction is predominantly linear up to 50 T for all the temperatures between 10 and 300 K (Fig. 10F). The fitted carrier density n is 3.28×10^{23} cm^{-3} at 300 K and decreases to 1.36×10^{23} cm^{-3} at 10 K through a slighter carrier freeze-out effect compared with the (110)-oriented RuO_2/MgO heterostructure.

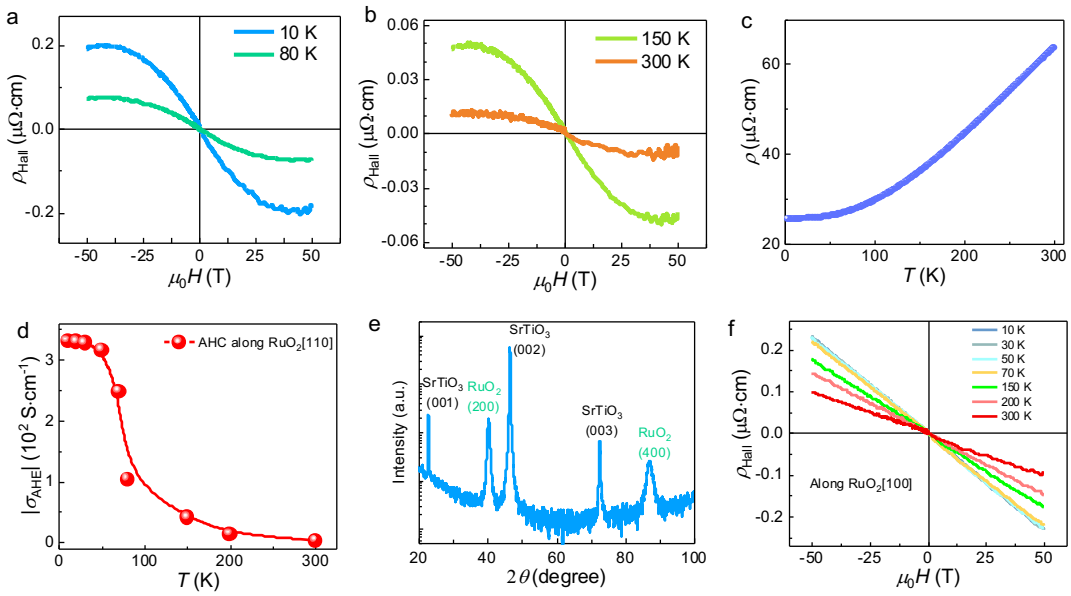

Figure 10: Hall effect along the out-of-plane direction of RuO2 thin films. (A)-(B), Hall effect up to 50 T measured for the (110)-oriented RuO2/MgO heterostructure at 10, 80, 150 and 300 K, respectively. (C) Resistivity versus temperature for the RuO2/MgO heterostructure. (D) The magnitude of anomalous Hall conductivity as a function of temperature for the RuO2/MgO heterostructure. (E) X-ray diffraction spectrum of a RuO2/SrTiO3 heterostructure, indicating a highly ordered (100) orientation of the RuO2 film. (F) Hall effect of the (100)-oriented RuO2/SrTiO3 heterostructure up to 50 T at different temperatures ranging from 10 to 300 K.

References

[1] Šmejkal, L., Železný, J., Sinova, J. & Jungwirth, T. Electric Control of Dirac Quasiparticles by Spin-Orbit Torque in an Antiferromagnet. *Physical Review Letters* **118**, 106402 (2017). URL `https://link.aps.org/doi/10.1103/PhysRevLett.118.106402`. `1610.08107`.

[2] Bodnar, S. Y. *et al.* Writing and reading antiferromagnetic Mn2Au by Néel spin-orbit torques and large anisotropic magnetoresistance. *Nature Communications* **9**, 348 (2018). URL `http://www.nature.com/articles/s41467-017-02780-x`. `arXiv:1706.02482`.

[3] Perdew, J. P., Burke, K. & Ernzerhof, M. Generalized gradient approximation made simple. *Physical Review Letters* **78**, 1396–1396 (1996). URL `https://link.aps.org/doi/10.1103/PhysRevLett.78.1396`. `0927-0256(96)00008`.

[4] Wadley, P. *et al.* Tetragonal phase of epitaxial room-temperature antiferromagnet CuMnAs. *Nature Communications* **4**, 2322 (2013). `1402.3624`.

[5] Wadley, P. *et al.* Antiferromagnetic structure in tetragonal CuMnAs thin films. *Scientific Reports* **5**, 17079 (2015).

[6] Schoop, L. M. *et al.* Dirac cone protected by non-symmorphic symmetry and three-dimensional Dirac line node in ZrSiS. *Nature Communications* **7**, 11696 (2016). `1509.00861`.

[7] Wadley, P. *et al.* Electrical switching of an antiferromagnet. *Science* **351**, 587–590 (2016). `1503.03765`.

[8] Tang, P., Zhou, Q., Xu, G. & Zhang, S.-C. Dirac fermions in an antiferromagnetic semimetal. *Nature Physics* **12**, 1100–1104 (2016). URL http://www.nature.com/articles/nphys3839. 1603.08060.

[9] Shi, W. *et al.* Prediction of a magnetic Weyl semimetal without spin-orbit coupling and strong anomalous Hall effect in the Heusler compensated ferrimagnet Ti2MnAl. *Physical Review B* **97**, 060406 (2018). URL https://link.aps.org/doi/10.1103/PhysRevB.97.060406. 1801.03273.

[10] Šmejkal, L., González-Hernández, R., Jungwirth, T. & Sinova, J. Crystal Hall effect in Collinear Antiferromagnets. *arXiv:1901.00445* (2019). URL https://lanl.arxiv.org/pdf/1901.00445http://arxiv.org/abs/1901.00445. 1901.00445.

[11] Feng, Z. *et al.* Observation of the Crystal Hall Effect in a Collinear Antiferromagnet (2020). URL http://arxiv.org/abs/2002.08712. 2002.08712.

[12] Nagaosa, N., Sinova, J., Onoda, S., MacDonald, A. H. & Ong, N. P. Anomalous Hall effect. *Reviews of Modern Physics* **82**, 1539–1592 (2010). 0904.4154.

[13] Shtrikman, S. & Thomas, H. Remarks on linear magneto-resistance and magneto-heat-conductivity. *Solid State Communications* **3**, 147–150 (1965). URL http://linkinghub.elsevier.com/retrieve/pii/003810986590178X.

[14] Kleiner, W. H. Space-time symmetry of transport coefficients. *Physical Review* **142**, 318–326 (1966).

[15] Seemann, M., Ködderitzsch, D., Wimmer, S. & Ebert, H. Symmetry-imposed shape of linear response tensors. *Physical Review B* **92**, 155138 (2015). URL https://link.aps.org/doi/10.1103/PhysRevB.92.155138. 1507.04947.

[16] Suzuki, M.-T., Koretsune, T., Ochi, M. & Arita, R. Cluster multipole theory for anomalous Hall effect in antiferromagnets. *Physical Review B* **95**, 094406 (2017). URL https://link.aps.org/doi/10.1103/PhysRevB.95.094406. 1611.06042.

[17] Grimmer, H. General relations for transport properties in magnetically ordered crystals. *Acta Crystallographica Section A* **49**, 763–771 (1993).

[18] Chen, H., Niu, Q. & Macdonald, A. H. Anomalous hall effect arising from noncollinear antiferromagnetism. *Physical Review Letters* **112**, 017205 (2014). 1309.4041.

[19] Kübler, J. & Felser, C. Non-collinear antiferromagnets and the anomalous Hall effect. *Epl* **108**, 67001 (2014). 1410.5985.

[20] Nakatsuji, S., Kiyohara, N. & Higo, T. Large anomalous Hall effect in a non-collinear antiferromagnet at room temperature. *Nature* **527**, 212–215 (2015).

[21] Nayak, A. K. *et al.* Large anomalous Hall effect driven by a nonvanishing Berry curvature in the noncolinear antiferromagnet Mn3Ge. *Science Advances* **2**, e1501870–e1501870 (2016). 1511.03128.

[22] Liu, E. *et al.* Giant anomalous Hall effect in a ferromagnetic kagome-lattice semimetal. *Nature Physics* **14**, 1125–1131 (2018). URL http://www.nature.com/articles/s41567-018-0234-5http://dx.doi.org/10.1038/s41567-018-0234-5.

[23] MacHida, Y., Nakatsuji, S., Onoda, S., Tayama, T. & Sakakibara, T. Time-reversal symmetry breaking and spontaneous Hall effect without magnetic dipole order. *Nature* **463**, 210–213 (2010).

[24] Shindou, R. & Nagaosa, N. Orbital ferromagnetism and anomalous hall effect in antiferromagnets on the distorted fcc lattice. *Physical Review Letters* **87**, 116801–1–116801–4 (2001). 0108322.

[25] Nagaosa, N. & Tokura, Y. Topological properties and dynamics of magnetic skyrmions. *Nature Nanotechnology* **8**, 899–911 (2013). URL http://www.nature.com/articles/nnano.2013.243.

[26] Sürgers, C., Fischer, G., Winkel, P. & Löhneysen, H. V. Large topological Hall effect in the non-collinear phase of an antiferromagnet. *Nature Communications* **5**, 3400 (2014). URL www.nature.com/naturecommunicationshttp://www.nature.com/articles/ncomms4400.

[27] Ghimire, N. J. *et al.* Large anomalous Hall effect in the chiral-lattice antiferromagnet CoNb3S6. *Nature Communications* **9**, 3280 (2018). URL www.nature.com/naturecommunicationshttp://www.nature.com/articles/s41467-018-05756-7.

[28] Suzuki, T. *et al.* Large anomalous Hall effect in a half-Heusler antiferromagnet. *Nature Physics* **12**, 1119–1123 (2016).

[29] Vistoli, L. *et al.* Giant topological Hall effect in correlated oxide thin films. *Nature Physics* **15**, 67–72 (2019). URL http://www.nature.com/articles/s41567-018-0307-5.

[30] IE Dzyaloshinskii. The Magnetic Structure of Fluorides of the Transition Metals. *Sov. Phys. JETP* **6**, 1120–1122 (1958).

[31] Gopalan, V. & Litvin, D. B. Rotation-reversal symmetries in crystals and handed structures. *Nature Materials* **10**, 376–381 (2011). 1007.3544.

[32] Berlijn, T. *et al.* Itinerant Antiferromagnetism in RuO2. *Physical Review Letters* **118**, 2–7 (2017). 1612.09589.

[33] Zhu, Z. H. *et al.* Anomalous Antiferromagnetism in Metallic <math display="inline"> <mrow> <msub> <mrow> <mi>RuO</mi> </mrow> <mrow> <mn>2</mn> </mrow> </msub> </mrow> </math> Determined by Resonant X-ray Scattering. *Physical Review Letters* **122**, 017202 (2019). URL http://arxiv.org/abs/1806.02036http://dx.doi.org/10.1103/PhysRevLett.122.017202https://link.aps.org/doi/10.1103/PhysRevLett.122.017202. 1806.02036.

[34] Takahashi, K. S. *et al.* Anomalous Hall effect derived from multiple Weyl nodes in high-mobility EuTiO 3 films. *Science Advances* **4**, eaar7880 (2018). URL http://advances.sciencemag.org/lookup/doi/10.1126/sciadv.aar7880.

[35] Zhang, H., Haule, K. & Vanderbilt, D. Metal-Insulator Transition and Topological Properties of Pyrochlore Iridates. *Physical Review Letters* **118**, 026404 (2017). 1505.01203.

[36] Kim, K. *et al.* Large anomalous Hall current induced by topological nodal lines in a ferromagnetic van der Waals semimetal. *Nature Materials* **17**, 1–6 (2018). URL http://www.nature.com/articles/s41563-018-0132-3.

[37] Chang, G. *et al.* Topological quantum properties of chiral crystals. *Nature Materials* **17**, 978–985 (2016). URL http://arxiv.org/abs/1611.07925http://dx.doi.org/10.1038/s41563-018-0169-3https://doi.org/10.1038/s41563-018-0169-3http://www.nature.com/articles/s41563-018-0169-3. 1611.07925.

[38] Gallego, S. V. *et al.* MAGNDATA: towards a database of magnetic structures. II. The incommensurate case. *J. Appl. Cryst* **49**, 1941–1956 (2016). URL http://dx.doi.org/10.1107/S16005767160154911941.

[39] Gerber, A. Interpretation of experimental evidence of the topological Hall effect. *Physical Review B* **98**, 214440 (2018). URL https://link.aps.org/doi/10.1103/PhysRevB.98.214440.

[40] Tokura, Y., Yasuda, K. & Tsukazaki, A. Magnetic topological insulators. *Nature Reviews Physics* **1**, 126–143 (2019). URL http://www.nature.com/articles/s42254-018-0011-5.